

---

# Point Cloud Sequence Encoding for Material-conditioned Graph Network Simulators

---

Philipp Dahlinger<sup>1\*</sup>

Balázs Gyenes<sup>1</sup>

Niklas Freymuth<sup>1</sup>

Luca Geminiani<sup>2</sup>

Tobias Würth<sup>3</sup>

Johannes Mitsch<sup>3</sup>

Nadja Klein<sup>2</sup>

Luise Kärger<sup>3</sup>

Gerhard Neumann<sup>1</sup>

<sup>1</sup>Autonomous Learning Robots, <sup>2</sup>Methods for Big Data, <sup>3</sup>Institute of Vehicle System Technology  
Karlsruhe Institute of Technology, Karlsruhe

## Abstract

Graph Network Simulators (GNSs) have emerged as powerful surrogates for complex physics-based simulation, offering inherent differentiability and orders-of-magnitude speedups over traditional solvers. However, GNSs typically assume access to the underlying material parameters, such as stiffness or viscosity, severely limiting their utility in realistic experimental settings. While recent meta-learning approaches address the parameter dependency by inferring properties from mesh trajectories, reconstructing a mesh from an observed scene is challenging. In this work, we introduce Point Cloud Encoding for Accurate Context Handling (*PEACH*), a novel framework that applies in-context learning on point clouds to adapt a learned simulator to unseen physical properties during inference. Our approach relies on a novel spatio-temporal point cloud sequence encoder, as well as two forms of auxiliary supervision to help improve simulation fidelity. We demonstrate that *PEACH* is capable of accurate zero-shot sim-to-real transfer on a challenging, dynamic scene. Experiments on simulation scenes show that *PEACH* even outperforms mesh-based baselines on prediction accuracy, while being much more practical for real-world deployment.

## 1 Introduction

Physics simulation is central to engineering disciplines ranging from structural mechanics to robotics, yet classical solvers based on the finite element method are computationally expensive [1, 2]. Graph Network Simulators (GNSs) have emerged as fast and differentiable surrogates for mesh-based physics, offering orders-of-magnitude speedups over classical solvers [3–7]. However, standard GNSs assume known process conditions, resulting in a parameter estimation problem when physical parameters change. Classical system identification can recover such parameters, but doing so per-instance multiplies the experimental and computational cost in ways that scale poorly [8–13]. Test-time gradient inversion through a differentiable simulator is one response, but reintroduces a per-instance optimization loop and there is no guarantee that the loss objective for inversion is well-conditioned [14, 15]. In-context conditioning instead amortizes identification by encoding a set of context trajectories into a latent material descriptor, enabling rapid adaptation to new material configurations at inference time [16]. In this work, we formulate adaptive physical simulation as a real-to-sim in-context learning problem. Using a novel spatio-temporal encoder architecture

---

\*Correspondence to philipp.dahlinger@kit.edu

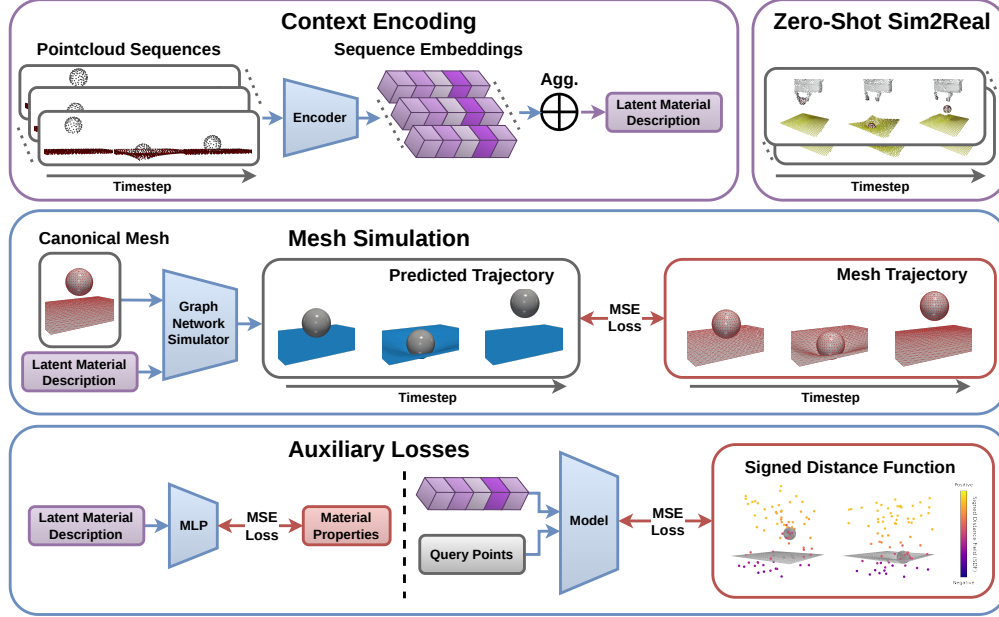


Figure 1: Overview of the Point Cloud Encoding for Accurate Context Handling (*PEACH*) framework. Point cloud sequences from several simulated or real trajectories are encoded into a single latent material description via our novel spatio-temporal encoder architecture. The aggregated latent vector conditions a mesh-based simulator, which predicts complete trajectories from an initial mesh. To improve accuracy, we apply auxiliary losses based on the ground truth physical properties and the Signed Distance Field (SDF). During inference, only the context point cloud sequences and an initial geometry are needed to simulate behavior with novel, unseen material properties.

proposal combines in-context conditioning for rapid adaptation with prediction of unknown physical parameters in a latent space to encode a more expressive and informative context as input for the simulator.

Operating on meshes instead of points [17, 18] helps GNSs generate stable and more accurate predictions over long sequences. However, mesh trajectories of arbitrary deforming objects are not directly observable with standard sensing; reconstructing them requires either invasive marker setups or template registration that itself depends on geometric and constitutive priors [19, 20]. Point clouds, in contrast, are produced directly by depth cameras and LiDAR and capture 3D geometry of deforming objects. Because they rely on geometric structure rather than surface appearance, sim-to-real transfer is less constrained by rendering fidelity [21–24]. While point cloud observations can easily be generated from meshes, point clouds from the real world do not contain correspondences between points from subsequent time steps. This complicates the estimation of physical parameters, since the motion of individual points contains the most information about those parameters. Unlike in mesh-based approaches, these correspondences must be inferred indirectly.

To address these challenges, we introduce Point Cloud Encoding for Accurate Context Handling (*PEACH*)<sup>2</sup>, an in-context framework that conditions a graph network simulator on a small set of observed point cloud sequences. This framework is able to predict mesh-level dynamics for unseen materials, without any test-time parameter optimization. *PEACH* extends the conditional neural process framework [25] to spatio-temporal observations: a spatio-temporal encoder maps each point cloud sequence to a latent vector, and the resulting set is aggregated into a single material descriptor that conditions the simulator. Our novel encoder architecture extends the common point-patch paradigm [26–28] by treating a sequence as a single point cloud embedded in 4D space-time. By relying on proximity in 4D space-time, the network can extract physical properties from the observation without explicit point-to-point correspondences. While this architecture is already competitive, we found in preliminary experiments that additional auxiliary losses can further improve the results. We investigate two auxiliary losses applied during training only: a regression head that

<sup>2</sup>Code and videos of rollouts are provided in the supplementary material. Datasets will be released upon acceptance.

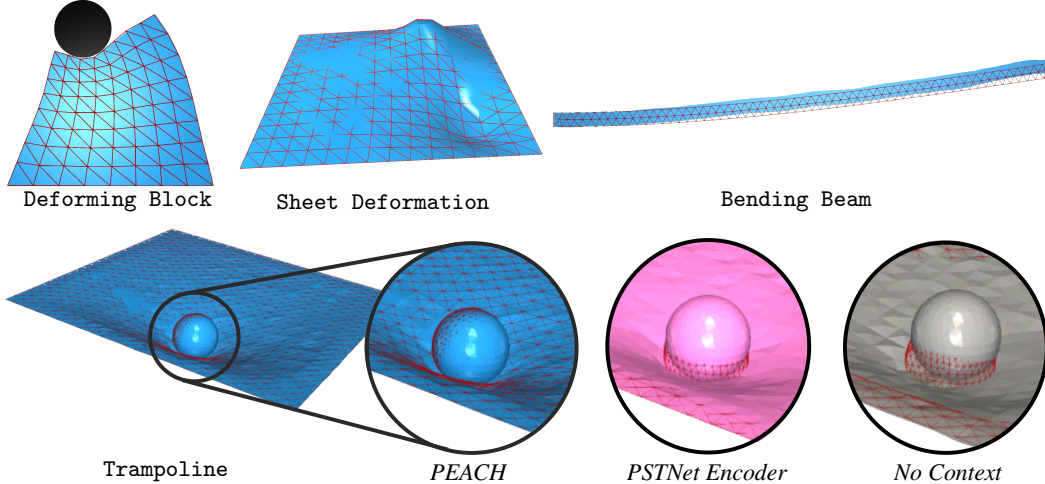


Figure 2: Overview of the four simulation scenes. The environments cover a range of deformable object types and material models, from purely elastic to viscoelastic constitutive behaviors, with varying material properties across tasks. Qualitative predictions of *PEACH* and selected baselines are shown in blue, pink, and gray, respectively, with ground-truth meshes overlaid in red.

grounds the latent embedding in the ground truth physical parameters, and a Signed Distance Field (SDF) reconstruction loss that encourages the encoder to retain fine-grained geometric information in the earlier layers. For inference, the model receives an initial mesh of the canonical geometry, which is typically available from CAD or a one-time scan, and 1 to 8 point cloud sequences from the target process. *PEACH* predicts the remaining mesh simulation using the implicit physical properties defined by the context.

To summarize, our contributions are as follows: (i) We propose *PEACH*, an end-to-end architecture that efficiently and accurately simulates a mesh-based trajectory conditioned on a handful of observed point clouds, without test-time optimization. As a key benefit, our novel spatio-temporal point cloud encoder is applicable to any operation on point cloud sequences due to its generality. (ii) We demonstrate *PEACH*'s sim-to-real capability through one-shot, rapid adaptation of a real-world scene in which a robot drops a ball onto a rubber trampoline, a setting beyond the reach of mesh-based methods. We additionally validate on four simulation scenes featuring deformable objects and outperform baselines with access to the ground truth context mesh. (iii) Through parameter studies, we provide insights that underscore the necessity of auxiliary losses for parameter regression and SDF. Furthermore, we visualize the latent space to show that it summarizes well the underlying physical properties of the scene.

## 2 Related Work

**System Identification.** Physical parameters such as stiffness or relaxation behavior are rarely known precisely for real-world scenes, which limits the use of Partial Differential Equation (PDE) simulators in many engineering applications [29–33]. System identification [8, 9] recovers such parameters from indirect observations. In applied mechanics, related approaches include finite element model updating and the Virtual Fields Method [34–36]. Recent approaches pair learned models with physics engines or differentiable simulators for property estimation and control [11–13], and train surrogate models for PDE-constrained parameter inference [14, 15, 37].

A different line of robotic real-to-sim work recovers deformable-object parameters via a per-instance test-time optimization. These works include iterative FEM-comparison [38], to differentiable rendering and simulation [39], to differentiable-simulator system identification on point clouds [40, 37]. Each instance requires a fresh optimization, which is typically done iteratively. The objective is non-convex and exhibits local minima and sloppy parameter directions [41, 42]. Direct-inversion alternatives sidestep the non-convexity but require dense full-field strain measurements [34] that are unavailable in typical real-world settings. *PEACH* amortizes identification into a learned encoder, replacing per-instance optimization with a single forward pass. Although our simulator is differen-

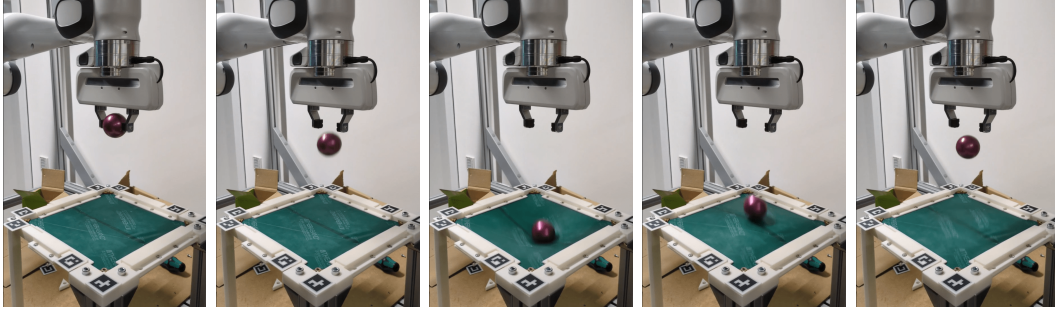


Figure 3: Real-world Trampoline setup. A robot arm releases a steel ball above an elastic membrane stretched across a 3D-printed frame, with ArUco markers at the corners for calibration.

tible, we avoid test-time optimization as it scales poorly across many instances and because the inverse problem is ill-conditioned [42], and instead rely on generalization from training data.

**Adapting Learned Simulators to New Materials.** Graph network simulators have emerged as fast, differentiable surrogates for mesh- and particle-based physics, enabling scalable simulation of physical systems of rigid bodies [3, 43], deformable solids [4], and PDE-like dynamics on unstructured meshes [5]. Recent extensions aim to capture long-range interactions in nonlinear solid mechanics via hierarchical architectures [44, 45, 7]. These methods assume known process conditions and thus inherit the parameter-estimation problem whenever materials change. Recent work therefore conditions learned simulators on material parameters either via parameter-efficient fine-tuning [46] or via meta-learning over a context set of trajectories [47, 48].

In particular, MaNGO [16] encodes a context set of mesh trajectories into a latent material descriptor that conditions a trajectory-level GNS, enabling adaptation to unseen materials in a single forward pass without test-time optimization. This is achieved via a Conditional Neural Process (CNP) formulation for in-context learning [25]. However, mesh trajectories of arbitrarily deforming objects are not directly observable with real-world sensors, limiting MaNGO to synthetic data regimes. Instead, we condition on point cloud sequences, enabling adaptive physical simulation of real scenes with readily available 3D cameras. Recent advances in foundation models for stereo reconstruction further support this approach by enabling the generation of cleaner and less noisy point clouds [49].

**Point Cloud Sequence Observations for Learned Simulators.** While permutation-invariant set encoders for individual point clouds [50, 51, 26–28] are well-established, processing point cloud sequences requires architectures that handle spatial irregularity and frame-to-frame motion without explicit point correspondences [52, 53]. Within learned simulation, point clouds have been used either to ground mesh-based GNSs in sensor observations [6], or as the basis of particle-based dynamics models that operate directly in observation space for deformable-object manipulation [54, 17]. In both cases, the latent physical properties are implicitly learned in the dynamics model, making adapting to new conditions less data efficient. Instant Policy [55] instead conditions imitation learning policies on point cloud demonstrations via amortized in-context learning. The method shares PEACH’s conditioning paradigm but applies to robot policies rather than material parameters and operates without a downstream physics simulator.

PEACH targets a regime not jointly addressed by prior work: amortized in-context sim-to-real adaptation from point cloud observations. It combines sequence-based point cloud encoders [52, 53] with in-context conditioning mechanisms [55, 16], while avoiding both the test-time optimization required by differentiable-simulator real-to-sim methods and the reliance on mesh-trajectory supervision in prior in-context simulator adaptation [16].

### 3 Point Cloud Encoding for Accurate Context Handling

**Problem Setting.** We consider a family of physical systems that share the same governing equations but differ in their physical properties, such as stiffness, damping, or thickness. The goal is to learn a simulator that mimics a Finite Element Method (FEM) solver and predicts a sequence of mesh states  $\hat{\mathcal{G}}_{1:T}$  at discrete frames  $1, \dots, T$ , without explicit knowledge of the physical properties  $\rho$ . This setup is common in industrial applications, where mesh-based representations are commonly available or

can be obtained through established reconstruction pipelines. In our work, each *task* corresponds to a fixed configuration of physical properties  $\rho$ , where the initial conditions such as mesh geometry or external forces may vary. For each initial condition, we generate a ground truth mesh trajectory using an FEM solver. By ray-tracing the mesh states with a virtual camera, we subsequently create an observed point cloud trajectory for each mesh trajectory. At inference, we wish to adapt our learned simulator to the given task, conditioned only on a small context of observed point cloud trajectories.

**Framework Overview.** During training, we sample a subset of  $C$  point cloud trajectories from one task, where each trajectory  $\mathcal{P}_i \in \mathbb{R}^{T \times N \times 3}$  consists of  $T$  frames of  $N$  points in 3D space. We encode each trajectory using a point cloud sequence encoder to obtain latent codes  $\{\mathbf{r}_1, \dots, \mathbf{r}_C\}$ , where each  $\mathbf{r}_c$  is a  $d_r$ -dimensional vector describing the physical properties from this trajectory in latent space. The per-sequence latent codes are further aggregated into a single task-level latent embedding  $\mathbf{r}$  of the physical properties via a learned softmax aggregation, enabling the model to handle a variable number of context trajectories. Concretely, given per-sequence latent codes  $\{\mathbf{r}_1, \dots, \mathbf{r}_C\}$ , the aggregated embedding is computed as

$$\mathbf{r} = \sum_{c=1}^C \alpha_c \odot \mathbf{r}_c, \quad \alpha_c = \frac{\exp(\beta \mathbf{r}_c)}{\sum_{c'=1}^C \exp(\beta \mathbf{r}_{c'})}, \quad (1)$$

where  $\beta$  is a learnable inverse-temperature parameter and the softmax is applied element-wise across the context dimension. Together with an initial mesh state  $\mathcal{G}_0$  sampled from the same task but independent of the context trajectories,  $\mathbf{r}$  is passed to a differentiable mesh-based simulator to predict the remaining trajectory  $\hat{\mathcal{G}}_{1:T}$ , supervised against the ground truth  $\mathcal{G}_{1:T}$ . The simulator is realized as a GNS. Gradients are propagated end-to-end through both the simulator and the point cloud encoder, ensuring that the learned physical representation is optimized for predictive accuracy.

At inference time, the material parameters  $\rho$  are unknown and only the mesh state  $\mathcal{G}_0$  of the initial configuration is available. The model must therefore rely entirely on the learned context encoding to estimate the material properties from a given sequence of context point clouds and simulate the resulting deformation. As we show in our experiments, the model is capable of generalizing to unseen physical properties in simulation and even to real data. Note that no real-world data is used for training, as neither ground truth mesh trajectories nor the true physical properties  $\rho$  are available. We next describe the graph network simulator used as the dynamics backbone of our framework.

**Graph Network Simulators.** GNSs generally follow one of two paradigms. Step-based simulators [4, 7] iteratively predict the next mesh state from the current one, which introduces a train-to-test gap due to error accumulation during rollout. Trajectory-based simulators [16, 48, 56] instead predict the entire remaining trajectory in a single forward pass, at the cost of higher memory requirements. *PEACH* utilizes the trajectory-based Meta Neural Graph Operator (*MaNGO*) simulator [16] there conditioning on the entire predicted trajectory, which we briefly review here for completeness.

Rather than maintaining separate graphs per timestep, *MaNGO* represents the trajectory as a single static graph  $\mathcal{G} = (\mathcal{V}, \mathcal{E})$  with temporally indexed node and edge feature tensors  $\mathbf{m}_v \in \mathbb{R}^{T \times |\mathcal{V}| \times d_{\text{node}}}$  and  $\mathbf{m}_e \in \mathbb{R}^{T \times |\mathcal{E}| \times d_{\text{edge}}}$ . The initial node features and trajectory-level conditioning variables, such as latent physical parameters, are broadcast across all time steps and augmented with a learned time embedding per timestep. Edge features are constructed from relative nodal positions. Both are then linearly projected into a latent dimension to obtain the initial feature tensors  $\mathbf{m}_v^0$  and  $\mathbf{m}_e^0$ . Spatial reasoning within each time step is performed via a message passing Graph Neural Network (GNN) layer, which updates node and edge features based on local neighborhood interactions:

$$\mathbf{m}_e^{k+1} = f_{\mathcal{E}}^k(\mathbf{m}_e^k, \mathbf{m}_v^k, \mathbf{m}_w^k), \text{ with } e = (v, w), \quad \tilde{\mathbf{m}}_v^{k+1} = f_{\mathcal{V}}^k(\mathbf{m}_v^k, \bigoplus_{e \in \mathcal{E}_v} \mathbf{m}_e^{k+1}).$$

Here,  $\mathcal{E}_v \subseteq \mathcal{E}$  denotes the edges incident to node  $v$ , and  $\bigoplus$  is a permutation-invariant aggregation. The functions  $f_{\mathcal{E}}^k$  and  $f_{\mathcal{V}}^k$  are learned Multilayer Perceptrons (MLPs).

The resulting node features  $\tilde{\mathbf{m}}_v^{k+1}$  are then processed independently over time by a 1D residual Convolutional Neural Network (CNN) to obtain  $\mathbf{m}_v^{k+1}$ . After  $K$  rounds of spatial message passing interleaved with temporal CNN processing, the model is trained by summing per-timestep Mean Squared Error (MSE) losses against ground truth mesh states over the full rollout. To condition the simulator on observed data, we require an encoder that maps point cloud trajectories into a compact representation of the underlying material properties.

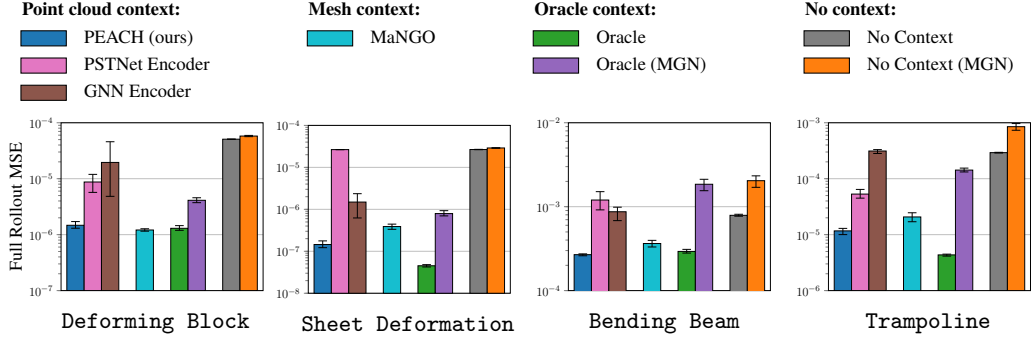


Figure 4: Simulation accuracy (MSE) on simulation datasets using 8 context trajectories. *PEACH* consistently outperforms other methods relying on point cloud observations for simulator adaptation. *PEACH* performs comparably to *MaNGO*, which uses privileged information in the form of meshes, and sometimes achieves performance competitive with the Oracle models.

**Spatio-Temporal Point Cloud Encoder.** The core challenge of the point cloud encoder is to compress a large number of spatially dense but informationally sparse points into a compact and expressive latent representation. Furthermore, there are numerous ways to treat a set of points across both space and time coordinates. While typical point-patch style encoders [26–28] are effective for tokenizing individual point clouds, material properties reveal themselves most clearly in the dynamics of the scene rather than in any single time step. Therefore, we adapt this paradigm to point cloud sequences and develop a novel encoder architecture by considering points in 4D space-time.

Space-time coordinates are computed by normalizing the sequence duration and applying a scaling factor of  $\tau$ . Setting  $\tau \rightarrow 0$  has the effect of ignoring the time axis, while  $\tau \rightarrow \infty$  recovers the case where each time step is encoded independently of all others. We sample  $M$  patch centers using Farthest Point Sampling (FPS) [51] and extract patches using K-Nearest Neighbors (KNN), both over space-time coordinates. We compute the features of each point using a Fourier feature projection [57, 58] of its space-time coordinates  $\gamma : \mathbb{R} \rightarrow \mathbb{R}^{2L}$  given by

$$\gamma_k(x) = \left[ \sin\left(\frac{2\pi x}{\lambda_k}\right), \cos\left(\frac{2\pi x}{\lambda_k}\right) \right]^T, \quad \lambda_k = \lambda_{\max} \left( \frac{\lambda_{\min}}{\lambda_{\max}} \right)^{\frac{k-1}{L-1}}, \quad k = 1, \dots, L,$$

where  $L$  is the number of frequency bands. The Fourier-encoded point features are concatenated with an additional object type feature, describing the object to which each point belongs. We use the PointMAE tokenizer [26] to get a patch embedding  $s \in \mathbb{R}^d$  from the point features of each patch, which is similar to PointNet [51] and uses max-pooling to aggregate over the patch. The point features of the patch center are passed through another MLP to yield a patch positional embedding  $c \in \mathbb{R}^d$ , which is then added to the patch embeddings to produce the patch tokens  $\mathbf{t} = s + c$ .

The  $M$  tokens  $\{\mathbf{t}_1, \dots, \mathbf{t}_M\}$  are passed into a transformer encoder, which refines them via self-attention. A final attention pooling layer compresses them into a single output token  $\mathbf{r}_i$  for the point cloud sequence  $\mathcal{P}_i$ . In contrast to simple mean or max pooling, the attention pooling layer uses a learned query token to attend over the transformer outputs, allowing the model to selectively focus on the most informative spatio-temporal regions. We found that a lightweight architecture with a single transformer layer suffices and outperforms deeper variants, suggesting that the tokenizer already captures most of the relevant structure and only light global reasoning is needed on top.

**Auxiliary Losses.** To encourage the latent representation to capture physically meaningful material properties and stabilize training, we introduce two auxiliary training objectives. As in *MaNGO*, we supervise the trajectory-level latent material description  $\mathbf{r}$  using ground-truth physical properties through a lightweight decoder  $\hat{\rho} = \text{MLP}(\mathbf{r})$ . The predicted  $\hat{\rho}$  can be interpreted as an explicit system identification of the current task.

We additionally supervise the patch tokenizer using an SDF objective inspired by Vosylius and Johns [55]. An SDF  $f : \mathbb{R}^3 \rightarrow \mathbb{R}$  assigns to each point  $\mathbf{p}$  its signed distance to the nearest mesh surface, with positive values outside and negative values inside. For 2D sheet-like geometries we treat the underside as interior. The distances are scaled and passed through a tanh nonlinearity to obtain normalized targets  $s = \tanh(\alpha f(\mathbf{p}))$ , which act similarly to truncation [59] and smoothly approach

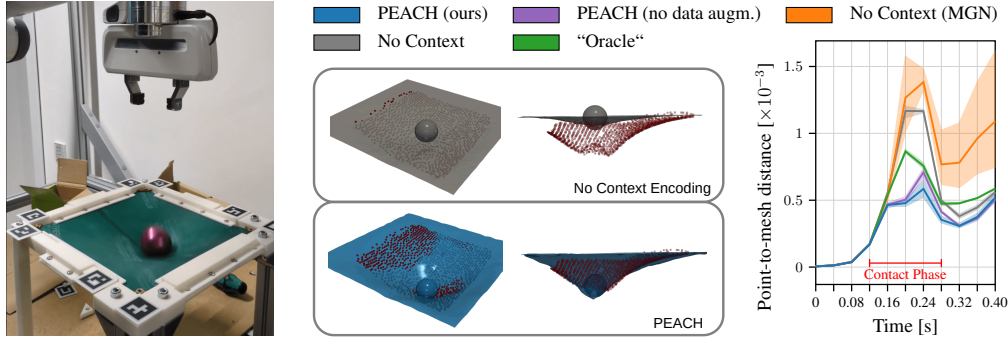


Figure 5: Real-world Trampoline scene. **Left:** Physical setup with a ball bouncing on a latex sheet. **Center:** Qualitative comparison at  $t=0.2$  s (maximal sheet stretching) between *PEACH* and a context-free simulator. The red point cloud shows the ground truth observations. The bottom of the sheet is occluded by the ball and thus absent from the point cloud. **Right:** Mean point-to-mesh distance over all real-world trials, plotted over time, with ball-sheet contact occurring in  $[0.12, 0.28]$  s.

an occupancy function [60] as  $\alpha \rightarrow \infty$ . For each trajectory and time step, we sample query points as visualized in the bottom right of Figure 1. For each query point, we find its  $K_{\text{SDF}}$  nearest patch tokens in 4D space-time and Fourier-encode their relative positions. These encodings are concatenated with the token embeddings and processed by an attention-based MLP that predicts a scalar weight per neighbor, biased by the normalized distance to emphasize spatio-temporal locality. A weighted aggregation of the features is decoded by a small MLP into a predicted signed distance, which is supervised against the ground-truth  $s$  using a smooth  $\ell_1$  loss.

**Data Augmentation.** To bridge the gap between simulated training data and real-world sensor inputs, we improve the robustness of the point cloud encoder via data augmentation. In particular, we perturb simulated point cloud sequences during training to mimic typical artifacts observed in real-world data. These augmentations include multi-scale Gaussian noise to model sensor uncertainty and structured region dropout [61] to simulate occlusions or missing observations. To account for sensor failures and reconstruction errors, we additionally inject sporadic point artifacts by sampling a small number of points uniformly from the scene’s bounding box. These augmentations enable generalization to noisy and incomplete point cloud observations, facilitating reliable material inference and simulation in real-world scenarios.

## 4 Experiments

**Scenes.** We evaluate the sim-to-real capability of *PEACH* on a novel scene called Trampoline that involves dynamic motion, complex contact interactions, and deformable objects. Additionally, we introduce the novel simulation-only dataset Bending Beam inspired by Würth et al. [7], and adopt two existing datasets, Deforming Block and Sheet Deformation [16]<sup>3</sup>. These scenes span 2D and 3D domains, and are inspired by simulation-assisted process optimization in industrial contexts. They feature varying physical parameters such as Young’s modulus (all except Deforming Block), Poisson’s ratio (all except Sheet Deformation), membrane thickness, shear relaxation ratio (Trampoline), and relaxation time (Bending Beam and Trampoline). Rollout length varies by scene from 25 (Trampoline) to 100 (Bending Beam). Although the Trampoline scene has a shorter horizon, it has the most complex geometry, with roughly 10 times more triangles than other scenes. A visual overview of the scenes is provided in Figure 2, with further details in Appendix C.

In simulation, we obtain per-step point clouds by ray casting from a static camera and applying FPS [51] to retain 512 points; due to the finer geometry Trampoline uses 1024 points. To reduce the point cloud sequence length, we drop every 2nd time step. In Trampoline and Deforming Block, collider points are explicitly marked. For the real world Trampoline dataset, we use a robot to drop balls of varying density onto latex sheets of different thicknesses and record depth images with a ZED Mini Stereo Camera (Stereolabs). Neither meshes nor ground truth physical parameters are known for these recordings. For the “Oracle” baseline, measurable material properties are

<sup>3</sup>Called Deformable Plate (*easy*) and Planar Bending, respectively, in Dahlinger et al. [16].

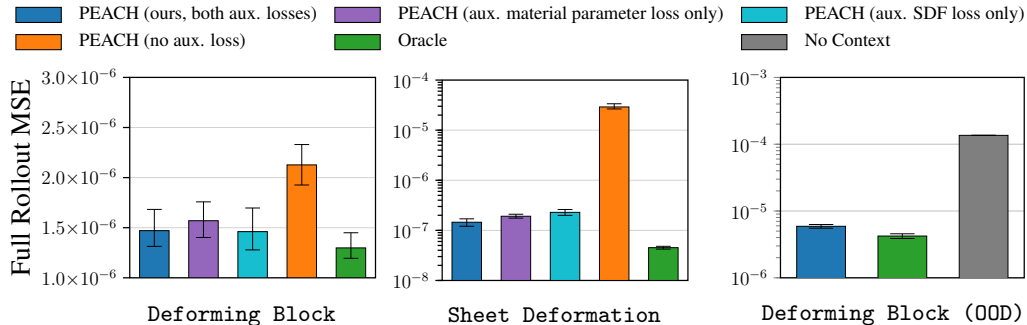


Figure 6: **Left, Center:** Ablation study of auxiliary losses in PEACH on the Deforming Block and Sheet Deformation environments, respectively. **Right:** Performance of PEACH on out-of-distribution test tasks for Deforming Block.

determined experimentally while the remaining parameters are chosen based on informed estimates from literature values. Further information on the real world data is in Appendix D.

**Baselines.** We compare *PEACH* against methods using 4 different context types: point cloud contexts, mesh contexts, oracle, and no context. Methods using point cloud contexts differ only in the encoder architecture used to encode point cloud sequences. *PSTNet Encoder* [53] captures local geometric evolution via space-time tubes anchored at FPS-sampled reference points, applying decoupled spatial and temporal convolutions hierarchically across the point cloud sequence. *GNN Encoder* adapts the graph network paradigm from mesh-based simulation to point cloud sequences. It tokenizes each timestep’s point cloud into local patch embeddings, constructs a spatio-temporal graph connecting tokens within and across adjacent frames, and processes it via message passing with a final readout into a trajectory-level latent code.

*MaNGO* [16] instead computes the latent embedding using privileged mesh contexts. Since such contexts are not readily available in real-world settings, *MaNGO* is not directly comparable to our method, but demonstrates the impact of replacing explicit mesh observations with point clouds in simulated tasks. *Oracle* methods receive the ground truth physical properties at every time step as additional node features. *No Context* methods predict trajectories solely from the initial state without additional task information. All baselines that predict a latent embedding also receive auxiliary supervision via ground truth physical properties.

Lastly, we study the impact of the simulator component by replacing the *MaNGO* simulator with the MeshGraphNet (MGN) simulator [4], a mesh-based autoregressive simulator trained for one-step prediction. We instantiate the MGN baseline in *Oracle (MGN)* and *No Context (MGN)* variants. While it is possible to integrate MGN into the *PEACH* framework, early experiments indicated that it was outperformed by the *MaNGO* simulator. Appendix B provides further details on baselines.

**Training.** We train each method end-to-end. All in-context methods are trained using batches of 1 to 8 randomly sampled context trajectories to improve adaptation capability. We repeat each experiment across 4 random seeds using the AdamW optimizer [62] with a learning rate of  $5.0 \times 10^{-5}$ . All methods were trained on either an A100 or H100 GPU for 2 days, with the exception of *Bending Beam*, which converged after 1 day. Appendix B.4 lists hyperparameters and Appendix B.3 provides runtime and parameter counts.

## 5 Results

**Simulation.** We evaluate the simulation fidelity using the MSE averaged across all steps in a complete rollout. Evaluation uses an in-distribution test split; both the physical properties as well as the initial conditions used for testing are unseen during training. Figure 4 shows that on simulation data, *PEACH* consistently outperforms all point cloud context methods by a substantial margin. Furthermore, *PEACH* outperforms the mesh-based *MaNGO* on three out of four environments, despite *MaNGO* operating on privileged mesh context. We attribute *MaNGO*’s underperformance to the relatively shallow CNN and Deep Sets architecture of its encoder, which limits its representational capacity. On *Bending Beam*, *PEACH* surpasses even the *Oracle* baseline. We attribute this to the expressiveness of the latent embedding of physical properties, which can jointly encode geometric

properties such as beam thickness alongside scalar material parameters, providing the simulator with a richer conditioning signal than the explicit oracle features alone. We note that replacing the simulator with the step-based MGN generally reduces accuracy, even with oracle information. Figure 2 shows qualitative predictions of *PEACH* across all four scenes, demonstrating accurate simulation of diverse physical behaviors over long time horizons. Additional qualitative results for all simulated tasks are provided in Appendix F.

**Real World.** Figure 3 shows an example trajectory of our real-world Trampoline setup. A robot arm releases a ball of unknown size and weight above an elastic membrane of varying thickness. Figure 5 demonstrates that *PEACH* is able to adapt to contexts from this real world setup without ever having seen real-world point clouds during training. Qualitatively, *PEACH* adapts to the interaction dynamics determined by the ball’s size and weight and the rubber sheet’s thickness, accurately capturing the sheet deformation at peak elongation. In contrast, the *No Context Encoding* baseline regresses to the mean, predicting only minimal deformation regardless of the physical parameters.

Quantitatively, *PEACH* outperforms all baselines, including the *Oracle* baseline where material parameters were measured directly from the physical setup. All methods perform well prior to ball-sheet contact, having learned to accurately predict free-fall dynamics, but baselines deteriorate significantly during the contact phase. Toward the end of the trajectory, prediction error increases across all methods, which we attribute to the inherently chaotic post-bounce behavior of the ball, whose direction after impact is difficult to predict deterministically. Combined, these results indicate our method’s ability to accurately simulate real-world scenes from only point cloud observations.

**Parameter Study.** We test the extrapolation capability of *PEACH* using an additional, out-of-distribution set of Deforming Block tasks in simulation. As illustrated in Figure 8 of the Appendix, test tasks are drawn from the tails of the Poisson ratio distribution, ensuring that the evaluated material properties lie outside the training range. Figure 6 (right) shows that *PEACH* remains close to the oracle performance even under this distribution shift, demonstrating that the learned latent material representation generalizes beyond the training distribution. A general analysis of performance as a function of context size is provided in Figure 9 of the Appendix E.

**Ablations.** Figure 6 (left, center) presents an ablation of the auxiliary losses on Deforming Block and Sheet Deformation. Removing both auxiliary losses leads to a substantial performance drop, confirming that auxiliary supervision is critical for learning a useful latent material representation. While *PEACH* benefits from combining both losses, training with only the SDF auxiliary loss remains competitive. Since SDF labels can be computed purely from mesh geometry, this is a practical option for settings where ground truth physical properties are unavailable. Figure 5 (right) contains an ablation of our method without data augmentation. Simulation accuracy is somewhat reduced in the post-bounce phase before falling again, indicating that data augmentation provides a small but meaningful improvement.

**Latent Space Analysis.** Figure 7 visualizes the PCA projection of the latent material codes encoded by *PEACH* on the Trampoline dataset. Despite no explicit structure being imposed on the latent space, the projection reveals a clear organization: the first principal component separates tasks by relaxation time, while the second separates them by loading ratio. This emergent disentanglement of physically meaningful material properties suggests that *PEACH* learns structured representations purely from point cloud observations. Latent space visualizations for all environments are provided in Figure 10 of the Appendix.

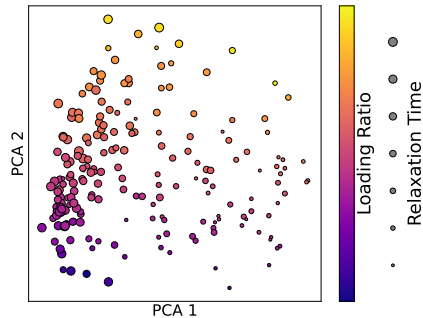


Figure 7: Visualization of the first and second PCA component of the latent space on the Trampoline dataset. Each point represents one simulation test task. Color corresponds to ratio of mass to product of Young’s modulus and sheet thickness, i.e., loading ratio, which governs the degree of sheet deformation. Size corresponds to relaxation time.

## 6 Conclusion

We present Point Cloud Encoding for Accurate Context Handling (*PEACH*), an in-context framework that conditions a graph network simulator on a handful of point cloud sequences to predict mesh-based

dynamics for unseen materials. By conditioning on point clouds instead of e.g., meshes, context data can be obtained easily from real world scenes. This allows *PEACH* to simulate real-world scenes without explicit parameter estimation or test-time optimization, and we demonstrate zero-shot sim-to-real transfer on a challenging trampoline scene. Across four challenging simulated datasets, *PEACH* performs on par with or better than mesh-based learned simulators, even when these have access to the ground truth parameters. Crucial to our method are our novel spatio-temporal encoder that treats context sequences as point clouds in 4D space-time, and auxiliary supervision in the form of direct parameter regression and prediction of SDF values.

**Limitations and future work.** *PEACH* assumes access to an initial scene geometry and requires context trajectories that share physical properties with the target process. Generating an initial mesh from observation would relax the geometry assumption, while accumulating context online during, e.g., robot execution would handle material drift across a process. Additionally, *PEACH* currently predicts the full trajectory in a single forward pass, which may impose memory constraints for long sequences and high-resolution meshes. Predicting sparse keyframes and training a separate network to interpolate between them is a promising way to decouple memory cost from horizon length. Further extensions could include other sensor modalities such as temperature readings and touch sensors for more accurate parameter estimation. We discuss broader impact in Appendix A.

## References

- [1] Olek C Zienkiewicz and Robert Leroy Taylor. *The finite element method for solid and structural mechanics*. Elsevier, 2005.
- [2] Eva Stanova, Gabriel Fedorko, Stanislav Kmet, Viero Slav Molnar, and Michal Fabian. Finite element analysis of spiral strands with different shapes subjected to axial loads. *Advances in engineering software*, 83:45–58, 2015.
- [3] Peter Battaglia, Razvan Pascanu, Matthew Lai, Danilo Jimenez Rezende, and koray kavukcuoglu. Interaction networks for learning about objects, relations and physics. In D. Lee, M. Sugiyama, U. Luxburg, I. Guyon, and R. Garnett, editors, *Advances in Neural Information Processing Systems*, volume 29. Curran Associates, Inc., 2016.
- [4] Tobias Pfaff, Meire Fortunato, Alvaro Sanchez-Gonzalez, and Peter W. Battaglia. Learning mesh-based simulation with graph networks. In *International Conference on Learning Representations*, 2021. URL <https://arxiv.org/abs/2010.03409>.
- [5] Johannes Brandstetter, Daniel E Worrall, and Max Welling. Message passing neural pde solvers. In *International Conference on Learning Representations*, 2022.
- [6] Jonas Linkerhägner, Niklas Freymuth, Paul Maria Scheikl, Franziska Mathis-Ullrich, and Gerhard Neumann. Grounding graph network simulators using physical sensor observations. In *The Eleventh International Conference on Learning Representations*, 2023.
- [7] Tobias Würth, Niklas Freymuth, Gerhard Neumann, and Luise Kärger. Diffusion-based hierarchical graph neural networks for simulating nonlinear solid mechanics. *Advances in Neural Information Processing Systems*, 39, 2025.
- [8] Karl Johan Åström and Peter Eykhoff. System identification—a survey. *Automatica*, 7(2): 123–162, 1971.
- [9] Ljung Lennart. System identification: theory for the user. *PTR Prentice Hall, Upper Saddle River, NJ*, 28:540, 1999.
- [10] Victor Isakov. *Inverse problems for partial differential equations*, volume 127. Springer, 2006.
- [11] Jiajun Wu, Ilker Yildirim, Joseph J Lim, Bill Freeman, and Josh Tenenbaum. Galileo: Perceiving physical object properties by integrating a physics engine with deep learning. *Advances in neural information processing systems*, 28, 2015.
- [12] J Krishna Murthy, Miles Macklin, Florian Golemo, Vikram Voleti, Linda Petrini, Martin Weiss, Breandan Considine, Jérôme Parent-Lévesque, Kevin Xie, Kenny Erleben, et al. gradsim: Differentiable simulation for system identification and visuomotor control. In *International conference on learning representations*, 2020.

- [13] Rika Antonova, Jingyun Yang, Krishna Murthy Jatavallabhula, and Jeannette Bohg. Rethinking optimization with differentiable simulation from a global perspective. In *Conference on robot learning*, pages 276–286. PMLR, 2023.
- [14] Qingqing Zhao, David B. Lindell, and Gordon Wetzstein. Learning to solve pde-constrained inverse problems with graph networks. 2022.
- [15] Tian Wang and Chuang Wang. Latent neural operator for solving forward and inverse PDE problems. In *The Thirty-eighth Annual Conference on Neural Information Processing Systems*, 2024. URL <https://openreview.net/forum?id=VLw8ZyKfcm>.
- [16] Philipp Dahlinger, Tai Hoang, Denis Blessing, Niklas Freymuth, and Gerhard Neumann. Mango—adaptable graph network simulators via meta-learning. *Advances in Neural Information Processing Systems*, 39, 2025.
- [17] Haochen Shi, Huazhe Xu, Samuel Clarke, Yunzhu Li, and Jiajun Wu. Robocook: Long-horizon elasto-plastic object manipulation with diverse tools. In Jie Tan, Marc Toussaint, and Kourosh Darvish, editors, *Conference on Robot Learning, CoRL 2023, 6-9 November 2023, Atlanta, GA, USA*, Proceedings of Machine Learning Research, pages 642–660. PMLR, 2023. URL <https://proceedings.mlr.press/v229/shi23a.html>.
- [18] William F Whitney, Jake Varley, Deepali Jain, Krzysztof Marcin Choromanski, Sumeet Singh, and Vikas Sindhwani. Modeling the real world with high-density visual particle dynamics. In *8th Annual Conference on Robot Learning*, 2024. URL <https://openreview.net/forum?id=pcPSGZFaCH>.
- [19] Elham Amin Mansour, Hehui Zheng, and Robert K. Katzschmann. Fast point cloud to mesh reconstruction for deformable object tracking. In Joaquim Filipe and Juha Röning, editors, *Robotics, Computer Vision and Intelligent Systems - 4th International Conference, ROBOVIS 2024, Rome, Italy, February 25-27, 2024, Proceedings*, Communications in Computer and Information Science, pages 391–409. Springer, 2024. doi: 10.1007/978-3-031-59057-3\_25. URL [https://doi.org/10.1007/978-3-031-59057-3\\_25](https://doi.org/10.1007/978-3-031-59057-3_25).
- [20] Matthew Loper, Naureen Mahmood, and Michael J. Black. Mosh: motion and shape capture from sparse markers. *ACM Trans. Graph.*, 33(6):220:1–220:13, 2014. doi: 10.1145/2661229.2661273. URL <https://doi.org/10.1145/2661229.2661273>.
- [21] Yuzhe Qin, Binghao Huang, Zhao-Heng Yin, Hao Su, and Xiaolong Wang. Dexpoint: Generalizable point cloud reinforcement learning for sim-to-real dexterous manipulation. In *6th Annual Conference on Robot Learning*, 2022. URL <https://openreview.net/forum?id=tJE1Yyi8fUX>.
- [22] Tsung-Wei Ke, Nikolaos Gkanatsios, and Katerina Fragkiadaki. 3d diffuser actor: Policy diffusion with 3d scene representations. In *8th Annual Conference on Robot Learning*, 2024. URL <https://openreview.net/forum?id=gqCQx0bVz2>.
- [23] Albert Wilcox, Mohamed Ghanem, Masoud Moghani, Pierre Barroso, Benjamin Joffe, and Animesh Garg. Adapt3r: Adaptive 3d scene representation for domain transfer in imitation learning. In *9th Annual Conference on Robot Learning*, 2025. URL <https://openreview.net/forum?id=sUW0SP6SUJ>.
- [24] Xiaogang Jia, Qian Wang, Anrui Wang, Han A. Wang, Balázs Gyenes, Emiliyan Gospodinov, Xinkai Jiang, Ge Li, Hongyi Zhou, Weiran Liao, Xi Huang, Maximilian Beck, Moritz Reuss, Rudolf Lioutikov, and Gerhard Neumann. Pointmappolicy: Structured point cloud processing for multi-modal imitation learning. In *The Thirty-ninth Annual Conference on Neural Information Processing Systems*, 2026. URL <https://openreview.net/forum?id=ZR2mdBrhJX>.
- [25] Marta Garnelo, Dan Rosenbaum, Christopher Maddison, Tiago Ramalho, David Saxton, Murray Shanahan, Yee Whye Teh, Danilo Rezende, and S. M. Ali Eslami. Conditional neural processes. *International Conference on Machine Learning*, 2018.
- [26] Yatian Pang, Wenxiao Wang, Francis EH Tay, Wei Liu, Yonghong Tian, and Li Yuan. Masked autoencoders for point cloud self-supervised learning. In *European Conference on Computer Vision*, pages 604–621. Springer, 2022.

- [27] Xumin Yu, Lulu Tang, Yongming Rao, Tiejun Huang, Jie Zhou, and Jiwen Lu. Point-bert: Pre-training 3d point cloud transformers with masked point modeling. In *Proceedings of the IEEE/CVF conference on computer vision and pattern recognition*, pages 19313–19322, 2022.
- [28] Guangyan Chen, Meiling Wang, Yi Yang, Kai Yu, Li Yuan, and Yufeng Yue. Pointgpt: Auto-regressively generative pre-training from point clouds. *Advances in Neural Information Processing Systems*, 36:29667–29679, 2023.
- [29] Lev Davidovich Landau, LP Pitaevskii, Arnold Markovich Kosevich, and Evgenii Mikhailovich Lifshitz. *Theory of elasticity: volume 7*, volume 7. Elsevier, 2012.
- [30] Jiri Blazek. *Computational fluid dynamics: principles and applications*. Butterworth-Heinemann, 2015.
- [31] Stjepan Salatovic, Sebastian Krumscheid, Florian Wittemann, and Luise Kärger. Reliable uncertainty quantification for fiber orientation in composite molding processes using multilevel polynomial surrogates. *Probabilistic Engineering Mechanics*, page 103806, 2025.
- [32] Stéphane Avril, Sam Evans, et al. *Material parameter identification and inverse problems in soft tissue biomechanics*, volume 573. Springer, 2017.
- [33] Boon Xian Chai, Maheshi Gunaratne, Mohammad Ravandi, Jinze Wang, Tharun Dharmawickrema, Adriano Di Pietro, Jiong Jin, and Dimitrios Georgakopoulos. Smart industrial internet of things framework for composites manufacturing. *Sensors*, 24(15):4852, 2024.
- [34] Stéphane Avril, Marc Bonnet, Anne-Sophie Bretelle, Michel Grédiac, François Hild, Patrick Jenny, Félix Latourte, Didier Lemosse, Stéphane Pagano, Emmanuel Pagnacco, et al. Overview of identification methods of mechanical parameters based on full-field measurements. *Experimental Mechanics*, 48(4):381–402, 2008.
- [35] Fabrice Pierron, Stéphane Avril, and V The Tran. Extension of the virtual fields method to elasto-plastic material identification with cyclic loads and kinematic hardening. *International Journal of Solids and Structures*, 47(22-23):2993–3010, 2010.
- [36] Marc Bonnet and Andrei Constantinescu. Inverse problems in elasticity. *Inverse problems*, 21(2):R1–R50, 2005.
- [37] Kaifeng Zhang, Baoyu Li, Kris Hauser, and Yunzhu Li. Adaptigraph: Material-adaptive graph-based neural dynamics for robotic manipulation. In Dana Kulic, Gentiane Venture, Kostas E. Bekris, and Enrique Coronado, editors, *Robotics: Science and Systems XX, Delft, The Netherlands, July 15-19, 2024*, 2024. doi: 10.15607/RSS.2024.XX.010. URL <https://doi.org/10.15607/RSS.2024.XX.010>.
- [38] Barbara Frank, Ruediger Schmedding, Cyrill Stachniss, Matthias Teschner, and Wolfram Burgard. Learning the elasticity parameters of deformable objects with a manipulation robot. In *2010 IEEE/RSJ International Conference on Intelligent Robots and Systems, October 18-22, 2010, Taipei, Taiwan*, pages 1877–1883. IEEE, 2010. doi: 10.1109/IROS.2010.5653949. URL <https://doi.org/10.1109/IROS.2010.5653949>.
- [39] Priya Sundaresan, Rika Antonova, and Jeannette Bohg. Diffcloud: Real-to-sim from point clouds with differentiable simulation and rendering of deformable objects. In *IEEE/RSJ International Conference on Intelligent Robots and Systems, IROS 2022, Kyoto, Japan, October 23-27, 2022*, pages 10828–10835. IEEE, 2022. doi: 10.1109/IROS47612.2022.9981101. URL <https://doi.org/10.1109/IROS47612.2022.9981101>.
- [40] Xintong Yang, Ze Ji, and Yu-Kun Lai. Differentiable physics-based system identification for robotic manipulation of elastoplastic materials. *The International Journal of Robotics Research*, 44(13):2126–2155, 2025.
- [41] Mark K Transtrum, Benjamin B Machta, and James P Sethna. Why are nonlinear fits to data so challenging? *Physical review letters*, 104(6):060201, 2010.

- [42] Yi Zhang, Albert Van Bael, Antonio Andrade-Campos, and Sam Coppieters. Parameter identifiability analysis: Mitigating the non-uniqueness issue in the inverse identification of an anisotropic yield function. *International journal of solids and Structures*, 243:111543, 2022.
- [43] Alvaro Sanchez-Gonzalez, Jonathan Godwin, Tobias Pfaff, Rex Ying, Jure Leskovec, and Peter Battaglia. Learning to simulate complex physics with graph networks. In *Proceedings of the 37th International Conference on Machine Learning*, pages 8459–8468. PMLR, 2020.
- [44] Youn-Yeol Yu, Jeongwhan Choi, Woojin Cho, Kookjin Lee, Nayong Kim, Kiseok Chang, ChangSeung Woo, ILHO KIM, SeokWoo Lee, Joon Young Yang, et al. Learning flexible body collision dynamics with hierarchical contact mesh transformer. In *The Twelfth International Conference on Learning Representations*, 2024.
- [45] Niklas Freymuth, Tobias Würth, Nicolas Schreiber, Balázs Gyenes, Andreas Boltres, Johannes Mitsch, Aleksandar Taranovic, Tai Hoang, Philipp Dahlinger, Philipp Becker, et al. Amber: Adaptive mesh generation by iterative mesh resolution prediction. In *The Thirty-ninth Annual Conference on Neural Information Processing Systems*, 2025.
- [46] Naveen Raj Manoharan, Hassan Iqbal, and Krishna Kumar. Parameter-efficient conditioning for material generalization in graph-based simulators. *arXiv preprint arXiv:2511.05456*, 2025.
- [47] Ankush Chakrabarty, Gordon Wichern, Vedang M Deshpande, Abraham P Vinod, Karl Berntorp, and Christopher R Laughman. Meta-learning for physically-constrained neural system identification. *Neurocomputing*, page 130945, 2025.
- [48] Philipp Dahlinger, Niklas Freymuth, Tai Hoang, Tobias Würth, Michael Volpp, Luise Kärger, and Gerhard Neumann. Context-aware learned mesh-based simulation via trajectory-level meta-learning. *Transactions on Machine Learning Research*, 2025.
- [49] Bowen Wen, Matthew Trepte, Joseph Aribido, Jan Kautz, Orazio Gallo, and Stan Birchfield. Foundationstereo: Zero-shot stereo matching. *arXiv*, 2025.
- [50] R. Qi Charles, Hao Su, Mo Kaichun, and Leonidas J. Guibas. Pointnet: Deep learning on point sets for 3d classification and segmentation. In *2017 IEEE Conference on Computer Vision and Pattern Recognition (CVPR)*, pages 77–85, 2017. doi: 10.1109/CVPR.2017.16.
- [51] Charles Ruizhongtai Qi, Li Yi, Hao Su, and Leonidas J Guibas. Pointnet++: Deep hierarchical feature learning on point sets in a metric space. In I. Guyon, U. Von Luxburg, S. Bengio, H. Wallach, R. Fergus, S. Vishwanathan, and R. Garnett, editors, *Advances in Neural Information Processing Systems*, volume 30. Curran Associates, Inc., 2017. URL <https://proceedings.neurips.cc/paper/2017/file/d8bf84be3800d12f74d8b05e9b89836f-Paper.pdf>.
- [52] Xingyu Liu, Mengyuan Yan, and Jeannette Bohg. Meteornet: Deep learning on dynamic 3d point cloud sequences. In *2019 IEEE/CVF International Conference on Computer Vision, ICCV 2019, Seoul, Korea (South), October 27 - November 2, 2019*, pages 9245–9254. IEEE, 2019. doi: 10.1109/ICCV.2019.00934. URL <https://doi.org/10.1109/ICCV.2019.00934>.
- [53] Hehe Fan, Xin Yu, Yuhang Ding, Yi Yang, and Mohan Kankanhalli. Pstnet: Point spatio-temporal convolution on point cloud sequences. In *International Conference on Learning Representations*, 2021.
- [54] Yunzhu Li, Jiajun Wu, Russ Tedrake, Joshua B. Tenenbaum, and Antonio Torralba. Learning particle dynamics for manipulating rigid bodies, deformable objects, and fluids. In *International Conference on Learning Representations*, 2019. URL <https://openreview.net/forum?id=rJgbSn09Ym>.
- [55] Vitalis Vosylius and Edward Johns. Instant policy: In-context imitation learning via graph diffusion, 2024. URL <https://arxiv.org/abs/2411.12633>.
- [56] Minkai Xu, Jiaqi Han, Aaron Lou, Jean Kossaifi, Arvind Ramanathan, Kamyar Azizzadenesheli, Jure Leskovec, Stefano Ermon, and Anima Anandkumar. Equivariant graph neural operator for modeling 3d dynamics. In *Forty-first International Conference on Machine Learning, ICML 2024, Vienna, Austria, July 21-27, 2024*. OpenReview.net, 2024. URL <https://openreview.net/forum?id=dccRCYmL5x>.

- [57] Matthew Tancik, Pratul Srinivasan, Ben Mildenhall, Sara Fridovich-Keil, Nithin Raghavan, Utkarsh Singhal, Ravi Ramamoorthi, Jonathan Barron, and Ren Ng. Fourier features let networks learn high frequency functions in low dimensional domains. *Advances in neural information processing systems*, 33:7537–7547, 2020.
- [58] Balázs Gyenes, Emiliyan Gospodinov, Jan Frieling, Enrico Krohmer, Xiaogang Jia, Nicolas Schreiber, Niklas Freymuth, and Gerhard Neumann. Fourier features let agents learn high precision policies with imitation learning. In *Forty-third International Conference on Machine Learning*, 2026. URL <https://openreview.net/forum?id=y03xxeUkgN>.
- [59] Brian Curless and Marc Levoy. A volumetric method for building complex models from range images. In *Proceedings of the 23rd annual conference on Computer graphics and interactive techniques*, pages 303–312, 1996.
- [60] Lars Mescheder, Michael Oechsle, Michael Niemeyer, Sebastian Nowozin, and Andreas Geiger. Occupancy networks: Learning 3d reconstruction in function space. In *Proceedings of the IEEE/CVF conference on computer vision and pattern recognition*, pages 4460–4470, 2019.
- [61] Terrance DeVries and Graham W Taylor. Improved regularization of convolutional neural networks with cutout. *arXiv preprint arXiv:1708.04552*, 2017.
- [62] Ilya Loshchilov and Frank Hutter. Decoupled weight decay regularization. In *7th International Conference on Learning Representations, ICLR 2019, New Orleans, LA, USA, May 6-9, 2019*. OpenReview.net, 2019. URL <https://openreview.net/forum?id=Bkg6RiCqY7>.
- [63] Chen Cai, Truong Son Hy, Rose Yu, and Yusu Wang. On the connection between mpnn and graph transformer. In *International Conference on Machine Learning*, pages 3408–3430. PMLR, 2023.
- [64] François Faure, Christian Duriez, Hervé Delingette, Jérémie Allard, Benjamin Gilles, Stéphanie Marchesseau, Hugo Talbot, Hadrien Courtecuisse, Guillaume Bousquet, Igor Peterlik, and Stéphane Cotin. SOFA: A Multi-Model Framework for Interactive Physical Simulation. In Yohan Payan, editor, *Soft Tissue Biomechanical Modeling for Computer Assisted Surgery*, volume 11 of *Studies in Mechanobiology, Tissue Engineering and Biomaterials*, pages 283–321. Springer, June 2012. doi: 10.1007/8415\_2012\_125. URL <https://hal.inria.fr/hal-00681539>.
- [65] Bowen Wen, Matthew Trepte, Joseph Aribido, Jan Kautz, Orazio Gallo, and Stan Birchfield. Foundationstereo: Zero-shot stereo matching. *CVPR*, 2025.

## A Broader Impact

*PEACH* is a method for simulating deformable objects from point cloud observations, aimed at making physics-based simulation more accessible when material properties are unknown or hard to measure. Efficient real-to-sim transfer of this kind could reduce reliance on costly physical experiments in engineering and scientific workflows and support digital twin construction for monitoring and design. It can additionally lower the barrier to high-fidelity simulation in domains such as biomechanics, materials science, and soft-body engineering, where calibrating constitutive models is traditionally laborious.

At the same time, any improvement in simulation fidelity carries dual-use potential, for instance in the design of weapons or other harmful artifacts. We view *PEACH* as a generic enabling technology in this regard, with no direct path to harm beyond what is already implied by progress in learned simulation more broadly. Like any data-driven model, *PEACH* may also inherit biases from its training distribution. In particular, materials, geometries, and process conditions that are underrepresented during training are likely to be predicted less accurately, which could lead to silent failures if the method is used outside its validated regime. We therefore encourage practitioners to validate *PEACH* on their target domain before relying on its predictions in decision-critical settings.

## B Methods and Hyperparameters

### B.1 Point Cloud Encoder

In this section, we provide additional details on the point cloud encoders used in our comparisons.

**PSTNet.** We closely follow the method proposed in [53] and use the official implementation and architecture from <https://github.com/hehefan/Point-Spatio-Temporal-Convolution>. The spatial kernel radius is adapted to 0.1 to match our task normalization, while all other architectural components and hyperparameters are kept unchanged.

**GNN Encoder.** At each timestep, we perform FPS to select 52 center points per point cloud in the sequence. For each center point, we connect its 16 nearest neighbors and apply a PointNet layer [50] to each resulting patch, yielding an embedding of dimension 32. We concatenate a Fourier encoding of the corresponding timestep to this embedding.

The resulting spatio-temporal tokens are then assembled into a graph: within each timestep, every node is connected to its 4 nearest neighbors. In addition, each node is connected to its 2 nearest neighbors in the subsequent timestep and to its single nearest neighbor in the following timestep. This construction yields a spatio-temporal graph encoding the complete point cloud sequence.

The graph is processed using a message-passing graph neural network [43] without global features, consisting of 5 layers with a latent dimension of 128. Finally, an attention-based readout module is applied to obtain a single output token.

### B.2 Mesh Encoder and Simulator

**Mango Mesh Encoder.** We closely follow the architecture of [16] and apply a one-dimensional convolutional neural network to each node along the temporal dimension. The mesh structure provides consistent point correspondences over time, enabling this temporal processing. Node features are then aggregated using a Deep Set architecture [63] to produce a permutation-invariant representation of the mesh. We use the official implementation, available at <https://github.com/ALRhub/mango>.

**Mango Simulator.** We closely follow the implementation from [16], using the official code available at <https://github.com/ALRhub/mango>.

### B.3 Parameters and Runtime

*PEACH* has a total of 3.96M parameters, of which 3.01M belong to the MaNGO simulator and 0.96M to the point cloud encoder and auxiliary loss heads.

Table 1: List of the used hyperparameters

Parameter	Value
Num Points in Pointcloud	512
Num Points in Pointcloud (Trampoline)	1024
FPS downsampling ratio (Tokenizer)	0.1
Patch size (Tokenizer)	16
Time scaling (Tokenizer)	16
Num. Fourier frequencies	8
Transformer Attention heads	4
Latent material representation dimension	128
Simulator Node feature dimension	128
Simulator Message passing blocks	15
Simulator Aggregation function	Mean
Simulator Activation function	Leaky ReLU
Optimizer	AdamW [62]
Learning rate	$5.0 \times 10^{-5}$
Weight decay	$1.0 \times 10^{-4}$
Min Context Size (Training)	1
Max Context Size (Training)	8
Latent representation aggregation	Learned Softmax
Auxiliary Loss Scale (Phys. Parameters)	0.02
Auxiliary Loss Scale (SDF)	0.5
Noise Scale MGN (Def. Block)	0.0007
Noise Scale MGN (Bend. Beam)	0.0007
Noise Scale MGN (Trampoline)	0.0005
Noise Scale MGN (Sheet Def.)	0.0005

We report inference timings on an NVIDIA RTX 5090 for the Trampoline environment. The encoding time scales with context size, ranging from 84 ms for a single context trajectory to 219 ms for eight.

The simulation rollout takes approximately 352 ms regardless of context size, as it operates solely on the aggregated latent code. In comparison, the FEM simulator used to generate the training data required 4 minutes per rollout on an AMD EPYC 74F3 24-Core Processor. Compared to classical system identification methods that require iterative test-time optimization, *PEACH* performs material inference in a single forward pass, making it orders of magnitude faster in practice.

#### B.4 Hyperparameters

We provide a list of the used hyperparameters in Table 1.

### C Simulation Datasets

This section provides detailed information about the datasets used in our experiments. The key characteristics of each dataset are summarized in Table 2. `Deforming Block` and `Sheet Deformation` consist of 16 simulation trials per task with various initial conditions, `Trampoline` and `Bending Beam` consist of 10 simulation trials per task.

Table 2: Dataset descriptions

Name	Train/Val/Test Splits	Number of Steps	Number of Nodes
Deforming Block	600/100/100	52	81
Sheet Deformation	460/50/50	50	225
Bending Beam	380/60/60	100	180
Trampoline	600/100/100	25	1700

### C.1 Trampoline.

This dataset models a thin square deformable sheet clamped by a rigid frame and deformed by a spherical impactor of varying size and density falling under gravity. Rigid body motion prediction of the ball is enforced by predicting per-node velocities and averaging them across all ball nodes. The sheet has initial stress-free edge length  $l_{\text{init}} = 245$  mm. The sheet is discretized by 9604 triangular membrane elements and 4901 nodes, with membrane thickness  $t$  varied as described below. To emulate the rigid frame in the physical setup, the sheet is pre-stretched to an edge length of  $l = 260$  mm by applying Dirichlet boundary conditions along its outer boundary.

Data generation follows a two-stage sampling procedure. In the first stage, a simulation configuration is defined by sampling the sheet material parameters together with the properties of a rigid spherical impactor. The sheet material is modeled as a nearly incompressible viscoelastic solid with rubber-like behavior. The instantaneous Young’s modulus is sampled uniformly from  $E \in [1, 5]$  MPa, the Poisson’s ratio is fixed to  $\nu = 0.499$ , and the membrane thickness is sampled from  $t \in [0.15, 0.4]$  mm. Rate dependence is modeled using a single-term Prony series with shear relaxation ratio  $g \in [0.01, 0.3]$  and relaxation time  $\tau \in [10^{-2}, 10^1]$  s. Volumetric relaxation is neglected ( $k = 0$ ). The impactor diameter is chosen from 15 to 55 mm in steps of 5 mm, with each diameter represented by a pre-meshed geometry of approximately 1000 elements. Its mass is sampled from  $[0.009, 0.269]$  kg, subject to density bounds between  $268 \text{ kg/m}^3$  (3D-printed PLA with 10% infill) and  $7850 \text{ kg/m}^3$  (steel). Gravitational loading is applied as an equivalent concentrated force at the impactor’s center of mass.

In the second stage, 10 trajectories are generated for each fixed stage-one configuration by varying only the initial conditions of the spherical impactor. Specifically, the in-plane drop position is sampled from a Gaussian distribution centered at the sheet origin and truncated to  $[-75, 75]$  mm in each in-plane direction, while the drop height is sampled within  $[120, 280]$  mm. Contact between the impactor and the sheet is modeled using hard normal contact to prevent interpenetration. Tangential contact is governed by a Coulomb friction law with coefficient  $\mu = 0.7$ . All simulations are performed in ABAQUS/EXPLICIT using explicit time integration.

### C.2 Bending Beam.

This scene consists of 2D beams clamped on the left side that bend and deform over time due to time-varying external forces applied on the right side. The beam is modeled as a rectangular domain embedded in two dimensional space. The left boundary of the beam is clamped with zero displacement, while external forces are applied to the right boundary. The load consists of one horizontal and one vertical force component. The horizontal force magnitude is sampled uniformly in  $[-1.0 \cdot 10^{-7}, 1.0 \cdot 10^{-7}]$ , while the vertical force magnitude is sampled uniformly in  $[-3.0 \cdot 10^{-5}, 3.0 \cdot 10^{-5}]$ . The forces are varied smoothly over time using cubic spline interpolation, starting from zero force, reaching the sampled target magnitude, and returning to zero before the end of the simulation. The beam height is sampled normally with mean 0.3 and standard deviation 0.01, and the beam length is sampled normally with mean 10.0 and standard deviation 1.0. The maximum characteristic mesh length, used for mesh generation, is sampled normally with mean 0.2 and standard deviation 0.02. The material behavior is modeled using an isotropic Kelvin–Voigt viscoelastic material model, combining an elastic stress response with a viscous stress contribution. Young’s modulus  $E$  is sampled log-uniformly in  $[0.5, 5.0]$ , Poisson’s ratio  $\nu$  is sampled uniformly in  $[0.0, 0.45]$ , and the viscosity parameter  $\tau$  is sampled log-uniformly in  $[0.05, 0.5]$ . Geometric nonlinearities due to large deformations are considered. The beam is discretized using linear triangular elements. The simulations are implemented in `scikit-fem` and solved using Newton iterations with a residual tolerance of  $10^{-8}$ . We create a total of 500 simulations, each consisting of 40,000 time steps. For the GNS, we subsample to 100 time steps per trajectory.

### C.3 Deforming Block.

This scene consists of 2D trapezoids deformed by a circular collider. This environment was originally implemented by Linkerhagner et al. [6] and uses Simulation Open Framework Architecture (SOFA) [64]. This dataset considers the deformation of a two dimensional rectangular block in two dimensional space. There are different trapezoidal initial geometries of the block. The nodes located at the bottom edge of the block are clamped with zero displacement. The load is applied by means of a

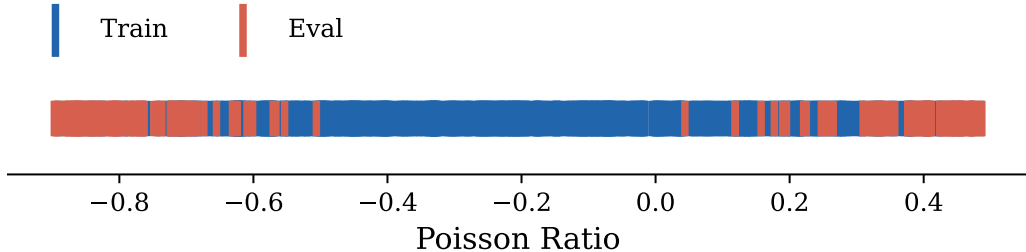


Figure 8: Out-of-distribution evaluation split for the Deforming Block OOD environment. Each tick marks one task, colored by split assignment. Eval tasks are drawn from the tails of the Poisson ratio distribution, ensuring that evaluated material properties lie outside the training range.

contact between a rigid circular collider and the top surface of the block. Across simulation trials, the collider radius is sampled uniformly between 10 % and 40 % of the block size and moves vertically downward at a constant velocity. The contact is modeled using a hard contact definition, which is rigid in the normal direction and frictionless in the tangential direction. The material behavior of the block is modeled using isotropic linear elasticity with a fixed Young’s modulus  $E$ , while the Poisson’s ratio  $\nu$  is sampled uniformly per task from  $[-0.9, 0.49]$ . The block is discretized using 81 nodes and 128 triangular elements.

The out-of-distribution evaluation split for this environment is visualized in Figure 8, where eval tasks are drawn from the tails of the Poisson ratio range  $[-0.9, 0.49]$ .

#### C.4 Sheet Deformation.

This dataset considers the deformation of a thin square 2D deformable sheet subjected to out-of-plane forces, resulting in 3D deformations. The sheet has initial stress-free edge length  $l = 140$  mm. The thickness of the sheet is intrinsically defined as  $t = 2.0$  mm. Nodes located at the outer edge of the sheet are clamped with zero displacement. The load is applied by two discrete external forces acting perpendicular to the thickness direction of the sheet. The force magnitude is fixed, while the normal force direction (upward or downward) and point of application are sampled uniformly. To enable a continuous range of force application locations, the forces are applied uniformly to all nodes within a small radius around the sampled application location. The forces are ramped up linearly from zero to their target magnitude over the simulated time. The material behavior of the sheet is modeled using isotropic linear elasticity with Young’s modulus  $E$  sampled log-uniformly in  $[10, 500]$  MPa and Poisson’s ratio  $\nu=0.3$ . The sheet is discretized using 225 nodes and 392 triangular elements. Geometric non-linearities due to large deformations are considered. The simulation for the described environment is implemented in the finite element software Abaqus/Standard and solved using implicit time integration.

## D Real World Experiments

We create a real-world version of **Trampoline** dataset for use in our sim to real experiments. To mimic the simulated scene, solid balls of various materials and densities (see Table 3) are dropped into rubber sheets of various thicknesses (see Table 4). The balls are dropped using a Franka Emika Panda robot, where the in-plane drop position is sampled from a volume of 4 cm x 4 cm x 5 cm. The scene is recorded using a StereoLabs Zed Mini stereo camera at a resolution of 720x1280 frame rate of 30 fps.

Depth estimates for each recorded frame are recomputed using FoundationStereo [65] (smaller architecture based on Vit-small). Images are resized to 480x853 and are converted into point clouds by unprojecting the depth using the cameras’ intrinsic parameters. The camera extrinsics are calibrated by mounting Aruco markers on the frame around the rubber sheet and optimizing for minimal reprojection error (OpenCV’s `solvePnP`). Point clouds are then transformed into a canonical world frame such that the bottom left corner of the sheet is at the origin and the sheet is on the xy plane.

Diameter (mm)	Mass (g)	Material
40	269	Steel Solid
40	69	Steel Hollow
50	110	Steel Hollow
60	162	Steel Hollow
40	21	PLA 50% Infill

Table 3: Sphere specifications used in the real-world experiments.

Color	Thickness (mm)	Average Density ( $\text{kg m}^{-3}$ )
Black	0.381	992.7
Green	0.254	992.7
Yellow	0.1524	992.7

Table 4: Sheet specifications used in the real-world experiments.

We discard time steps before the ball begins to fall and limit trajectories to 20 time steps (approx. 0.667 s). Points in the background of the scene are cropped out, and voxel downsampling is applied with a voxel edge length of 5 mm. To remove spurious artifacts, any points that have fewer than 20 neighbours within a radius of 15 mm are filtered out. Finally, FPS [51] is applied to reduce the point clouds to 2048 points.

Sphere points are identified via color segmentation, isolating the distinctly colored ball from the scene. The color labels are refined through an iterative algorithm that updates each point’s label based on its own color and the colors of its neighbors, smoothing spurious misclassifications at object boundaries. Given the known sphere diameter, a spherical mask is fitted to the identified sphere points by optimizing the center position, which is then used to remove robot arm points that fall outside the mask. Finally, FPS is applied to reduce the point clouds to 1024 points.

## E Additional Quantitative Results.

We provide full rollout MSE as a function of context size for all four environments in Figure 9. *PEACH* consistently improves with more context trajectories and achieves performance competitive with the Oracle baselines, while outperforming all point cloud-based methods across environments.

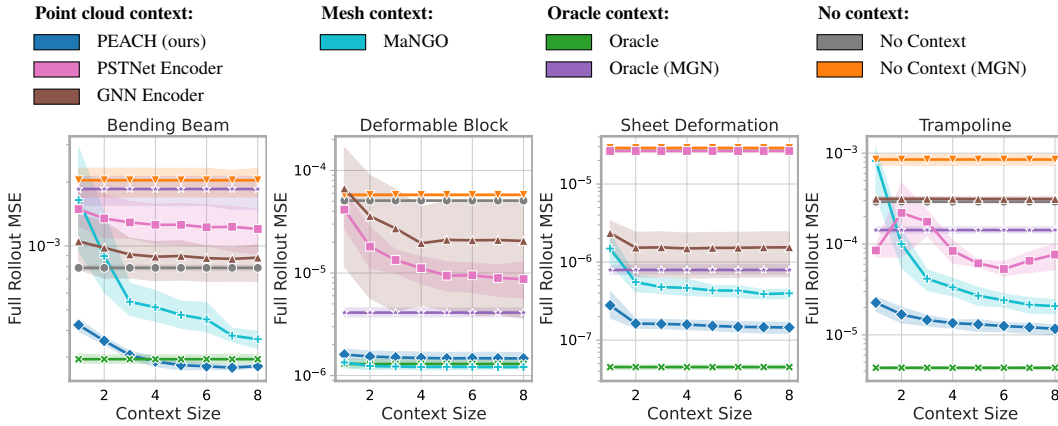


Figure 9: Full simulation rollout MSE across different baselines using 8 context trajectories. *PEACH* consistently performs similarly to the mesh-based MaNGO, improving over other point cloud-based baselines and achieving performance competitive with the Oracle models.

## F Visualizations

We provide additional qualitative results comparing all evaluated methods on both datasets.

### F.1 Latent Space Visualizations

Figure 10 shows a PCA projection of the task-level latent codes  $\mathbf{r}$  produced by the *PEACH* encoder across all four environments. Each point corresponds to a single test task, colored by its material properties. The smooth, structured organization of the latent space, particularly the near-perfect one-dimensional manifold recovered for the single-parameter environments Sheet Deformation and Deforming Block, demonstrates that the encoder successfully disentangles material properties from trajectory-level variation, without any explicit supervision on the latent space geometry.

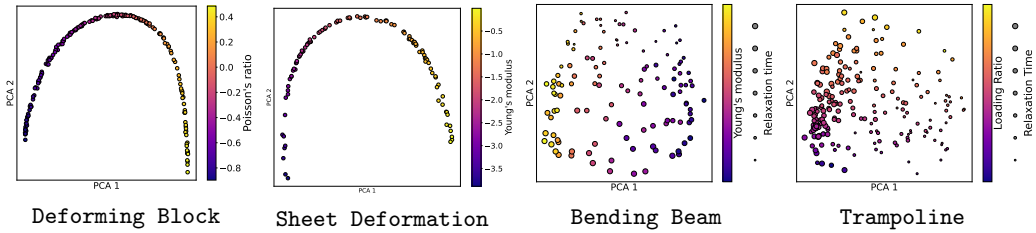


Figure 10: PCA visualization of the latent space on the Deforming block, Sheet deformation, Bending beam and Trampoline environment (left to right). Each point represents an encoded task, with different coloring and scaling references based on the task's material properties.

### F.2 Qualitative Trajectory Predictions

We provide qualitative trajectory predictions for all evaluated datasets. Figure 11 shows results for the Deforming Block dataset, Figure 12 for Sheet Deformation, Figure 13 for the Trampoline dataset, and Figure 14 for Bending Beam.

## Deforming Block

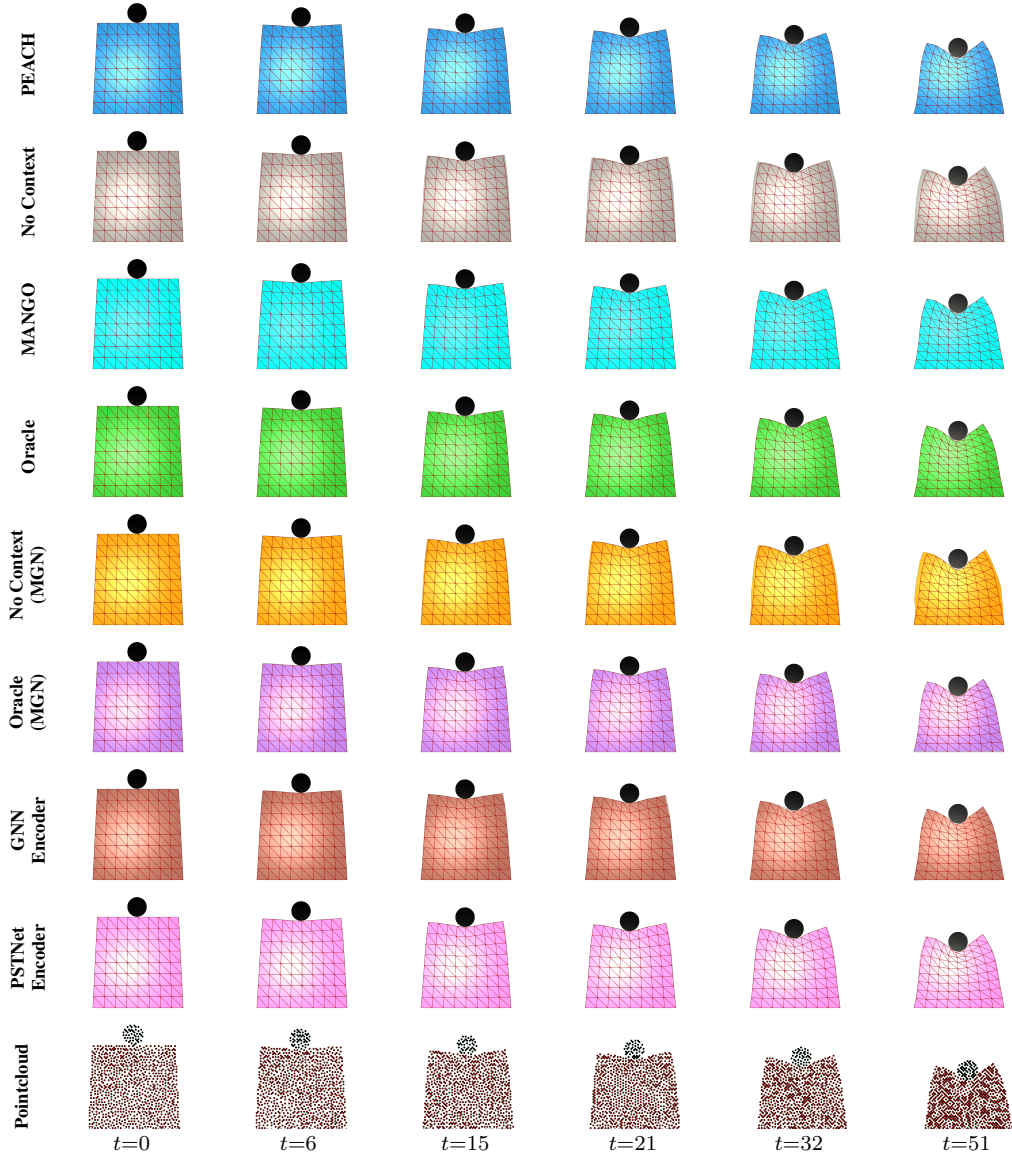


Figure 11: Predicted simulation of a Deforming Block test task by PEACH (blue), No Context (gray), MANGO (cyan), Oracle (green), No Context (MGN) (orange), Oracle (MGN) (purple), GNN Encoder (brown), and PSTNet Encoder (pink). All visualizations show the colored **predicted mesh**, a **collider**, and a **wireframe** (red) of the ground-truth simulation. The last row shows an exemplary point cloud sequence from the context set.

## Sheet Deformation

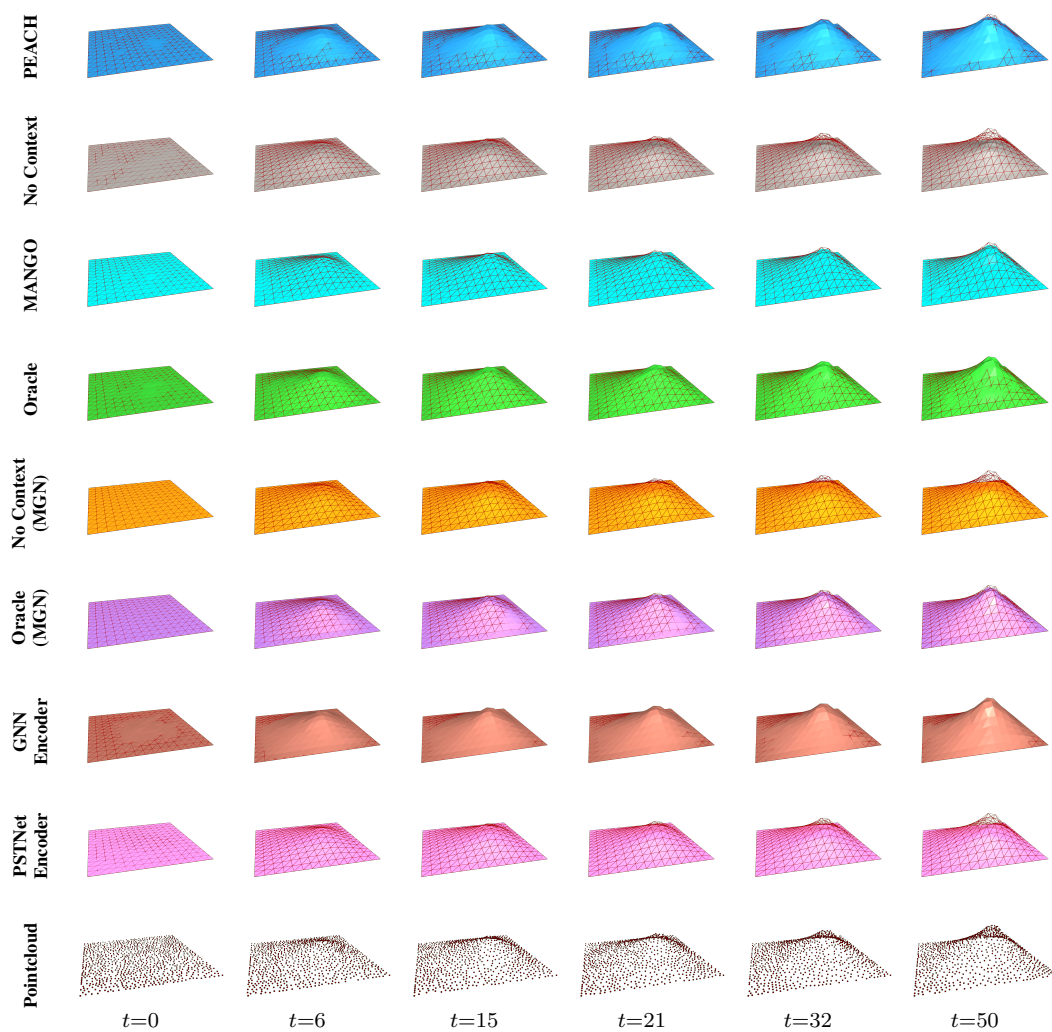


Figure 12: Predicted simulation of a Sheet Deformation test task by PEACH (blue), No Context (gray), MANGO (cyan), Oracle (green), No Context (MGN) (orange), Oracle (MGN) (purple), GNN Encoder (brown), and PSTNet Encoder (pink). All visualizations show the colored **predicted mesh** and a **wireframe** (red) of the ground-truth simulation. The last row shows an exemplary point cloud sequence from the context set.

## Trampoline

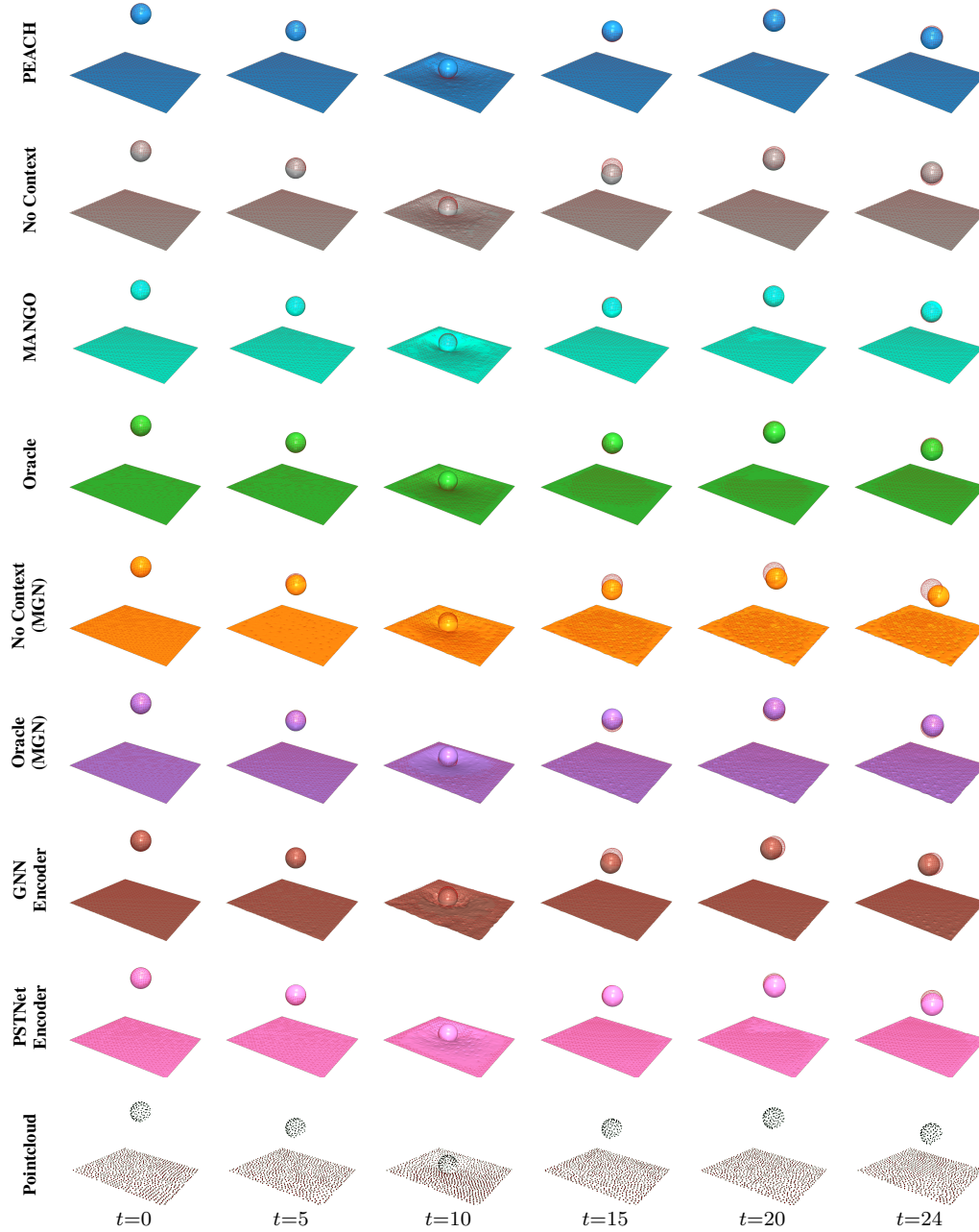


Figure 13: Predicted simulation of a Trampoline test task by PEACH (blue), No Context (gray), MANGO (cyan), Oracle (green), No Context (MGN) (orange), Oracle (MGN) (purple), GNN Encoder (brown), and PSTNet Encoder (pink). All visualizations show the colored **predicted mesh** and a **wireframe** (red) of the ground-truth simulation. The last row shows an exemplary point cloud sequence from the context set.

## Bending Beam

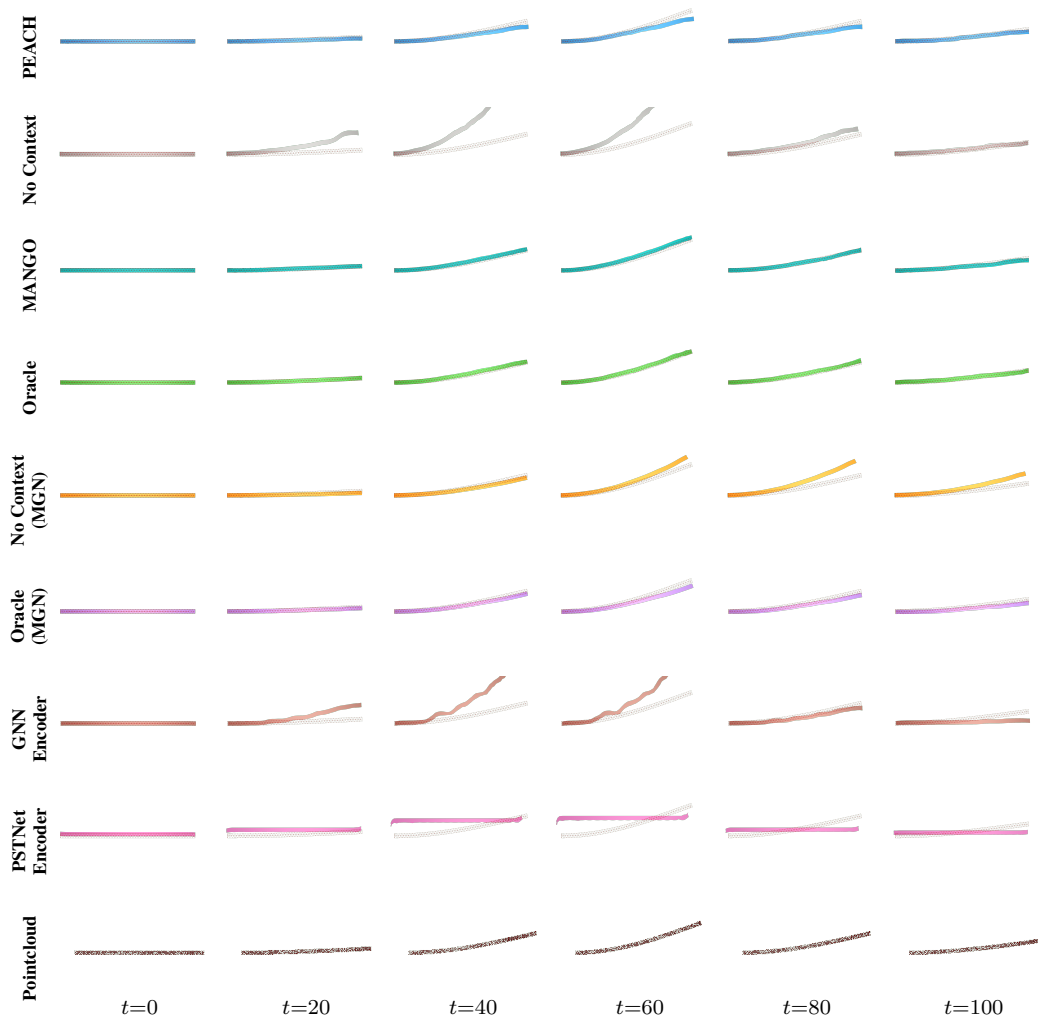


Figure 14: Predicted simulation of a Bending Beam test task by PEACH (blue), No Context (gray), MANGO (cyan), Oracle (green), No Context (MGN) (orange), Oracle (MGN) (purple), GNN Encoder (brown), and PSTNet Encoder (pink). All visualizations show the colored **predicted mesh** and a **wireframe** (red) of the ground-truth simulation. The last row shows an exemplary point cloud sequence from the context set.